Acta Pharmaceutica Sinica B 2014;4(1):52–59

Chinese Pharmaceutical Association
Institute of Materia Medica, Chinese Academy of Medical Sciences

Acta Pharmaceutica Sinica B

www.elsevier.com/locate/apsb
www.sciencedirect.com

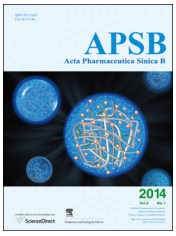

ORIGINAL ARTICLE

Three-dimensional DEM–CFD analysis of air-flow-induced detachment of API particles from carrier particles in dry powder inhalers

Jiecheng Yang[a,b,*], Chuan-Yu Wu[b], Michael Adams[a]

[a]*School of Chemical Engineering, University of Birmingham, Birmingham B15 2TT, UK*
[b]*Department of Chemical and Process Engineering, University of Surrey, Guildford GU2 7XH, UK*

Received 24 September 2013; revised 15 October 2013; accepted 14 November 2013

KEY WORDS

Dry powder inhaler;
Dispersion;
Detachment;
Air flow;
DEM–CFD

Abstract Air flow and particle–particle/wall impacts are considered as two primary dispersion mechanisms for dry powder inhalers (DPIs). Hence, an understanding of these mechanisms is critical for the development of DPIs. In this study, a coupled DEM–CFD (discrete element method–computational fluid dynamics) is employed to investigate the influence of air flow on the dispersion performance of the carrier-based DPI formulations. A carrier-based agglomerate is initially formed and then dispersed in a uniformed air flow. It is found that air flow can drag API particles away from the carrier and those in the downstream air flow regions are prone to be dispersed. Furthermore, the influence of the air velocity and work of adhesion are also examined. It is shown that the dispersion number (*i.e.*, the number of API particles detached from the carrier) increases with increasing air velocity, and decreases with increasing the work of adhesion, indicating that the DPI performance is controlled by the balance of the removal and adhesive forces. It is also shown that the cumulative Weibull distribution function can be used to describe the DPI performance, which is governed by the ratio of the fluid drag force to the pull-off force.

*Corresponding author at: School of Chemical Engineering, University of Birmingham, Birmingham B15 2TT, UK. Tel.: +44 7528533634.
E-mail addresses: jxy147@bham.ac.uk, yangjiecheng1113@gmail.com (Jiecheng Yang).

Peer review under responsibility of Institute of Materia Medica, Chinese Academy of Medical Sciences and Chinese Pharmaceutical Association.

Production and hosting by Elsevier

2211-3835 © 2014 Chinese Pharmaceutical Association and Institute of Materia Medica, Chinese Academy of Medical Sciences. Production and hosting by Elsevier B.V. Open access under CC BY-NC-ND license.
http://dx.doi.org/10.1016/j.apsb.2013.11.003

1. Introduction

Using dry powder inhalers (DPIs), active pharmaceutical ingredient (API) particles with diameters of *ca.* 5 μm can be directly delivered to the lung or respiratory tracts[1,2]. However, the flowability of fine API particles is poor owing to strong particle adhesion[3]. Therefore, API particles need to be either agglomerated to large granules that are subsequently de-agglomerated, or "carried" by other large particles then detached from the carrier particles, during the inhalation process[4]. Owing to the complicated nature of the process, the efficiency of current DPIs is low (*i.e.*, fine particle fraction (FPF) is normally less than 30%[2]). Generally, DPI performance is determined by the design of the device (*e.g.*, grid structure, mouthpiece length and geometry)[5–7], the formulation and the patients' respiration manoeuvre[4]; a number of studies have recently been performed to investigate the dependency of DPI performance on these factors[8,9]. The influence of formulation properties on DPI performance, such as particle size[10], particle concentration[11], particle morphology[12], particle surface roughness[13], density and porosity[14], crystal form[15], electrostatic charge[16], flowability[17] and the type of ternary additive,[18] has also been explored. The DEM or DEM–CFD approach was also applied to investigate the effects of impacts among particles/agglomerates/walls[19], fluid flow[20], particle adhesion[21] and device design[22].

Despite the above work, inconsistent results exist and the understanding of the dispersion process and relative importance of the contributory factors is still unclear. For example, it was reported that air flow can dominate the dispersion performance[23–25] while particle–particle and particle–wall impacts were also found to play an important role in the dispersion process of DPIs[26–28].

Voss and Finlay[23] developed a powder de-agglomeration device, which was designed to entrain a dose of powder into the air stream and expose the powder to either a controllable level of turbulence or a mesh; the objective was to explore the effects of turbulence and mechanical impaction on dry powder de-aggregation. They found that the extent of de-aggregation increased as the level of turbulence was increased. de Boer et al.[24] investigated the rate at which API particles are detached from carrier particles in adhesive mixtures in an air classifier, and found that the rate increased with increasing flow rate and dispersion time. Aerodynamic dispersion of loose aggregates in a uniform fluid flow was investigated using DEM–CFD by Calvert et al.[25]. They found that there was a threshold velocity above which dispersion occurred quickly and approached equilibrium asymptotically. These works explored the influence of air flow on the DPI detachment process; however, they were generally concerning the overall behaviour of the DPIs and the mechanical analysis of dispersion behaviour of loose agglomerate (*i.e.*, drug-only formulations). The investigation for carrier-based DPIs at the micro-mechanical level was hardly reported.

On the other hand, the effect of particle–particle and particle–wall impact on the dispersion behaviour of DPIs was also explored. Wong et al.[26] investigated the influence of turbulence on the break-up and aerosol performance of DPI formulations using a combination of computational fluid dynamics and standardized entrainment tubes. They argued that there was no correlation between the extent of the turbulence and aerosol performance and the impact dominated agglomerate break-up in the system considered. The influence of the impact on DPI performance was further examined by Wong et al.[27], who found that particle–wall impacts resulted in initial agglomerate fragmentation, followed by re-entrainment in the airstream. Tong et al.[28] applied a combined CFD and DEM approach and investigated powder dispersion. In their study, agglomerates of different particle sizes and poly-dispersities were dispersed in a cyclonic flow at different flow velocities. It was shown that the dispersion was governed by particle–wall impacts and particle–particle adhesion.

Nevertheless, the influence of air flow on the DPI dispersion and the dispersion mechanism still need further investigation. Therefore, the objective of this study is to investigate the effects of air flow on the detachment process for carrier-based DPIs. A coupled DEM–CFD is used to explore both gas–particle interactions and particle–particle adhesion. The effects of air velocity, work of adhesion and initial positions of API particles are examined and a mechanism governing the detachment performance is proposed.

2. Methods

2.1. Numerical models

The coupled DEM–CFD model developed by Kafui et al.[29] is used in this study, in which particle adhesion is analysed using the JKR theory[30] that was implemented by Thornton and Yin[31]. The translational and rotational motions of a particle are governed by Newton's second law:

$$m_i\frac{\mathrm{d}v_i}{\mathrm{d}t} = f_{\mathrm{ci}} + f_{\mathrm{api}} + m_i g \tag{1}$$

$$I_i\frac{\mathrm{d}\omega_i}{\mathrm{d}t} = T_i \tag{2}$$

where m_i, I_i, v_i and ω_i are the mass, moment of inertia, translational and rotational velocities of particle i, respectively. f_{ci}, f_{api} and T_i are the particle–particle/wall contact force, air–particle interaction force and torque acting on the particle, respectively. g is the gravitational acceleration.

Since the sizes of API particles are small, particle adhesion becomes significant. According to the JKR theory, for the adhesion between particles, a "pull-off" force, F_{c}, is defined as

$$F_{\mathrm{c}} = \frac{3}{2}\Gamma\pi R \tag{3}$$

where Γ is the thermodynamic work of adhesion and R is the effective radius, which are defined as

$$\Gamma = \gamma_1 + \gamma_2 - \gamma_{12} \tag{4}$$

$$R = \frac{r_1 \times r_2}{r_1 + r_2} \tag{5}$$

where γ and r are the surface energies and radii of two particles, 1 and 2.

The air–particle interaction force, according to Anderson and Jackson[32], can be obtained from:

$$f_{\mathrm{api}} = -v_{\mathrm{pi}}\nabla p + v_{\mathrm{pi}}\nabla\cdot\tau + \varepsilon f_{\mathrm{di}} \tag{6}$$

where v_{pi} is the volume of particle i, and p, τ, ε and f_{di} are local air pressure, viscous stress tensor, void fraction and drag force on particle i, respectively. According to Di Felice's correlation[33], f_{di}

can be obtained by

$$f_{\mathrm{di}} = \frac{1}{2} C_{\mathrm{Di}} \rho_{\mathrm{a}} \frac{\pi d_{\mathrm{pi}}^2}{4} \varepsilon^2 \left| u - v_i \right| (u - v_i) \varepsilon^{-(\chi+1)} \tag{7}$$

where C_{Di} and d_{pi} are the fluid drag coefficient and the diameter of the particle i, and ρ_{a} and u are the density and the velocity of the air, respectively. The determination of C_{Di} and χ can be found in Ref. 33.

The continuity and momentum equations for the fluid phase are given as follows:

$$\frac{\partial(\varepsilon \rho_{\mathrm{a}})}{\partial t} + \nabla \cdot (\varepsilon \rho_{\mathrm{a}} u) = 0 \tag{8}$$

$$\frac{\partial(\varepsilon \rho_{\mathrm{a}} u)}{\partial t} + \nabla \cdot (\varepsilon \rho_{\mathrm{a}} u u) = -\nabla p + \nabla \cdot \tau - F_{\mathrm{ap}} + \varepsilon \rho_{\mathrm{a}} \mathrm{g} \tag{9}$$

where F_{ap} is the air–particle interaction force per unit volume and can be obtained by

$$F_{\mathrm{ap}} = \left(\sum_{i=1}^{n_{\mathrm{c}}} f_{\mathrm{api}} \right) / \Delta V_{\mathrm{c}} \tag{10}$$

where n_{c} is the total number of particles in a fluid cell and ΔV_{c} is the volume of the fluid cell.

2.2. *Model setup*

Initially, a carrier particle with a radius R and 242 API particles with radii r randomly positioned around the carrier are generated (Fig. 1a). Then the API particles are set to move towards the centre of the carrier at a specified velocity until they attach to the carrier and reach a stable state (Fig. 1b). The work of adhesion between the carrier particle and API particles is initially set to a relatively high value during this attachment process and then reduced to the required value that is used for the simulation. Thereafter, the carrier–API agglomerate is subject to a uniform flow field with a specific velocity V and gravity is introduced; consequently, both the carrier particle and the API particles move due to the resultant forces. The fluid domain is 1260 μm long, 1260 μm wide and 2100 μm high. The lower boundary is set as the gas inlet velocity, and the upper boundary is set as a continuous outflow outlet, whereas the other boundaries are set as non-slip impermeable walls. The fluid cell size is twice as large as the size of the carrier. The particle and fluid properties used in the simulation are listed in Table 1. It is assumed that the carrier and API particles have the same material properties as that of α-lactose monohydrate[34]. Owing to the relatively small air flow rate in current cases, small works of adhesion are chosen, which are still comparable with the experimental results measured using AFM by Louey et al.[35], ranging from 0.3 to 0.9 mJ/m^2.

To quantify the detachment behaviour, a series of new parameters are introduced, including the contact number, N_{c}, dispersion number, N_{d}, retention ratio, ϕ, and dispersion ratio, Φ. The contact number N_{c} is defined as the number of API particles attaching to the carrier and the dispersion number as the number of API particles detached from the carrier. The retention ratio ϕ is then defined as the ratio of the contact number, N_{c}, to the initial number of API particles, N:

$$\phi = N_{\mathrm{c}} / N \tag{11}$$

The dispersion ratio is defined as the ratio of the dispersion number, N_{d}, to the initial number of API particles, N:

$$\Phi = N_{\mathrm{d}} / N \tag{12}$$

Table 1 Particle and fluid properties.

Parameter	Value
R (μm)	26.25–52.5
r (μm)	2.5
Particle density (kg/m^3)	2650
Young's modulus (GPa)	24
Poisson's ratio	0.3
Coefficient of friction	0.3
Work of adhesion (mJ/m^2)	0.1–0.6
Air velocity V (m/s)	1.0–4.0
Air pressure (kPa)	101.325
Air density (kg/m^3)	1.2
Air viscosity (kg/m·s)	1.8×10^{-5}

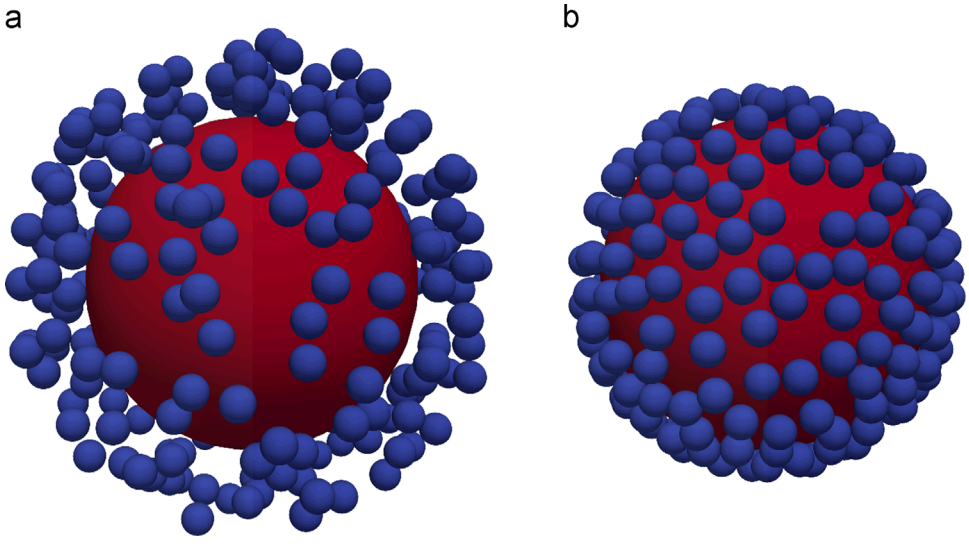

Figure 1 The agglomeration process: (a) initial setup and (b) prepared carrier–API agglomerate.

3. Results

Fig. 2 shows a typical detachment process at different time instants. In Fig. 1b, API particles are randomly attached to the carrier surface before air flow is introduced. When the air flow is introduced, the API particles in the downstream regions are removed directly (Fig. 2a). Meanwhile, the API particles in the middle regions move (either slide or roll) around the carrier to the downstream regions and then detach from the carrier (Fig. 2b and c). Thereafter, most API particles are detached from the carrier while the API particles in the upstream regions are not removed and still in contact with the carrier (Fig. 2d).

The evolution of the contact number with time at different air velocities is shown in Fig. 3, for which the carrier radius and the work of adhesion are set as 26.25 μm and 0.2 mJ/m^2, respectively. The time is normalized by the time of the dispersion process, which is the time period from the moment that gas is introduced to the moment that the agglomerate reaches the top boundary. It can be seen from Fig. 3 that the contact number decreases initially and then remains stable. It indicates that the air flow causes detachment of the API particles from the carrier as soon as it is introduced. This is attributed to the rapid acceleration of the agglomerate by the air flow. This dispersion mechanism was also reported by Gotoh et al.[36], who analysed the forces acting on the agglomerate in a uniformed flow and suggested that rapid acceleration or deceleration was the dispersion mechanism. It is also clear that the contact number decreases as the air velocity is increased, which suggests that an air flow with a large velocity, which causes large accelerations, can detach more particles from the carrier.

The effects of air velocity and work of adhesion on the dispersion ratio are shown in Fig. 4. The dispersion ratio increases with increasing air velocity, and decreases with increasing work of adhesion. This is consistent with the experimental observation of de Boer et al.[24] who reported that the amount of API detached from the carrier increased with the flow rate. It is also found that for a smaller work of adhesion, the dispersion ratio can reach a stable state at a lower air velocity, while for a larger work of adhesion, there is a threshold air velocity above which air flow can cause the detachment of the API particles from the carrier. This demonstrates that more API particles can be detached from the carrier by air flow at a higher velocity due to the larger fluid drag force. On the other hand, API particles with higher works of adhesion are more difficult to remove due to the strong inter-particle adhesion.

The distribution of contact normal orientations for the carrier particle is presented in Fig. 5, which shows the polar histogram[37] of the proportion of contact normal orientations falling within a series of adjacent orientation classes that partition the full orientation space. The unit circle representing the 0–360° full orientation space is partitioned into twelve bands in order to accommodate the contact normal orientations for the contacts between the carrier and API particles. Each contact is interrogated to identify its location in one of the twelve bands. If a contact is located in band i, the total contact number for this band is

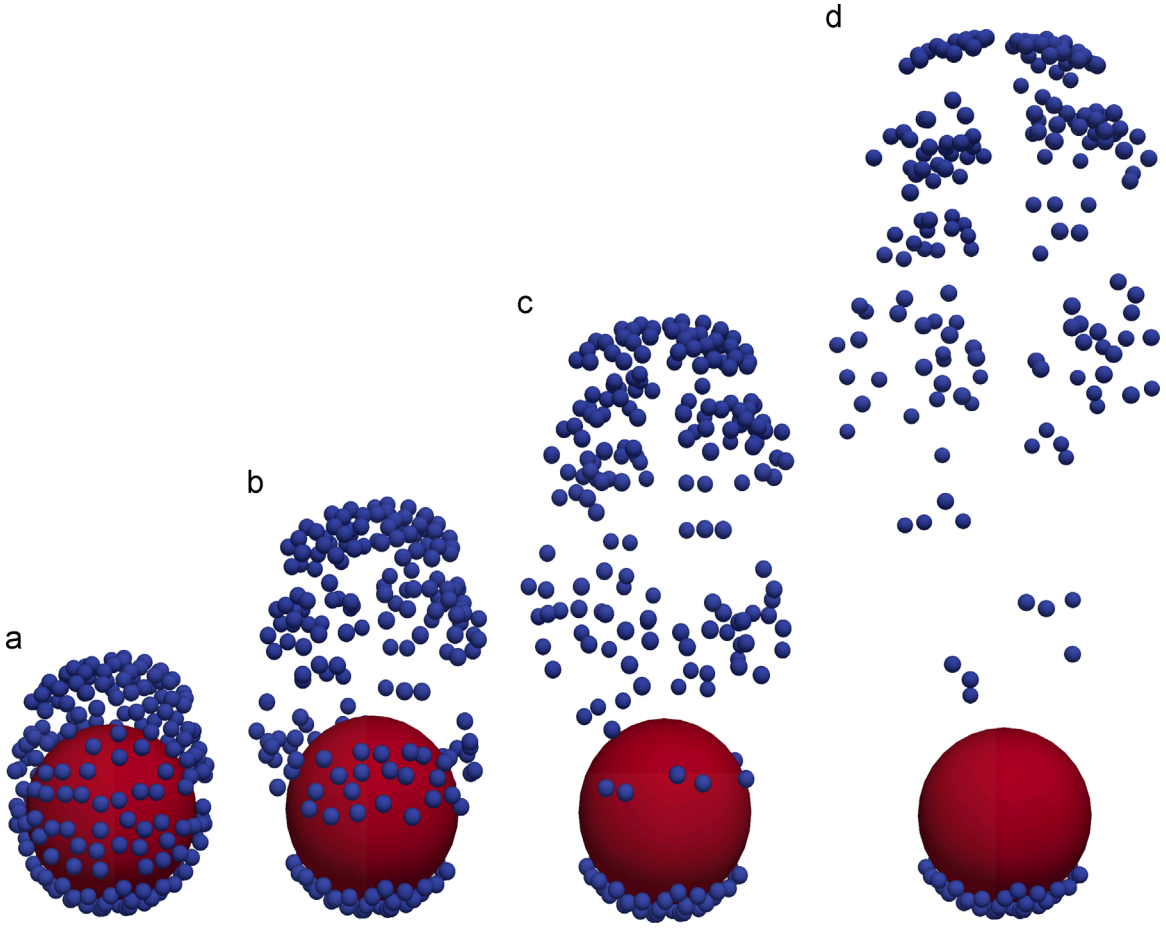

Figure 2 The detachment process at various time instants. (a) $t=4.55\times10^{-5}$ s; (b) $t=9.09\times10^{-5}$ s; (c) $t=1.36\times10^{-4}$ s; (d) $t=2.05\times10^{-4}$ s.

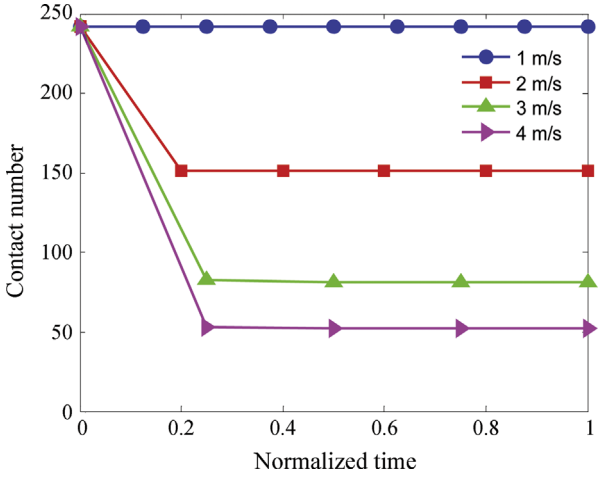

Figure 3 The time evolution of contact number at different air velocities (R=26.25 μm, Γ=0.2 mJ/m^2).

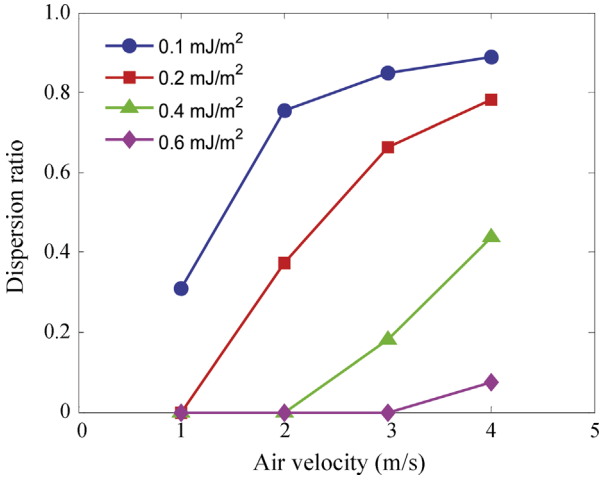

Figure 4 The variation of the dispersion ratio with air velocity for different works of adhesion (R=26.25 μm).

increased by one. After all contacts have been scanned, the contact number of band i when the dispersion process is completed, n_i, and the original contact number of band i when the agglomerate is formed, N_i can be obtained. The radial coordinate of band i, r_i is then determined as

$$r_i = \frac{n_i}{N_i} \tag{13}$$

referring to Eq. (11), r_i is equal to the retention ratio for band i.

It can be seen from Fig. 5a that the retention ratio in each band is equal to 1, indicating that no API particle detaches from the carrier when the air velocity is small. With an increase of the air velocity (Fig. 5b and c), the retention ratios in the downstream bands decrease, indicating that an increasing number of API particles detach from these regions. When the air velocity is high (Fig. 5d), the retention ratios in the downstream bands are equal to 0, corresponding to all the API particles in the downstream region being detached, and only the API particles in the upstream regions being still attached. That is, as the air velocity is increased, the retention ratios of the downstream regions decrease sharply while those in the upstream regions are stable. This phenomenon indicates that the API particles in the downstream regions are more likely to be removed by air flow. It could be a useful guide for engineered formulations that would be based on locating the API particles in specific areas to improve the overall efficiency of the DPIs.

A comparison of initial positions and detachment positions for API particles is shown in Fig. 6. The location of an API particle is quantified by the angle between the normal contact orientation and the vertical direction. The initial angle is that when the agglomerate is formed and the detachment angle is that when the API particle detaches. The initial and detachment angles of the detached particle are illustrated by hollow dots, whereas those of the attached particles are plotted with solid triangles. It is clearly shown that, for the API particles in the downstream regions (*i.e.*, regions with small initial angles), the initial and detachment positions are the same, which suggests that the API particles can be directly removed by the air flow after it is introduced; for the API particles near the equator, the detachment angles are smaller than the initial angles, which suggests that the API particles first move around the carrier to the downstream region and then detach from the carrier; the API particles in the upstream regions cannot be removed.

4. Discussion

The detachment process is governed by the removal force (*e.g.*, fluid drag force) and the adhesive force (*e.g.*, inter-particle force), and the dispersion performance is the result of the balance of these two forces. The variations of the dispersion ratio, Φ, with the fluid drag force (Eq. (7)) and the pull-off force (Eq. (3)) are shown in Fig. 7a and b, respectively. For each carrier size, cases with four air velocities and four works of adhesion, as shown in Table 1, are systematically simulated. It can be seen from Fig. 7a that for a specific fluid drag force, the dispersion ratio varies as the works of adhesion are different, indicating that the detachment process is not governed by the fluid drag force only. In addition, the variation range of dispersion ratio increases with increasing drag force, suggesting that API particles are more easily removed by high-speed flow. Similarly, it is clearly seen from Fig. 7b that for a specific pull-off force, the dispersion ratio varies with different air velocities. The variation range of the dispersion ratio decreases with increasing pull-off force, indicating that API particles are more difficult to be removed with strong adhesion. However, for either of the two figures, the data cannot superimpose into a master curve, which indicates that there is no direct correlation between the dispersion ratio and the removal force or the adhesive force.

Since the dispersion ratio, Φ, is a result of the balance of the removal and the adhesive forces, it is plotted as a function of the ratio of these two forces, $\eta = F_d/F_c$, as shown in Fig. 8. The data for all cases considered superimpose into a single master curve that can be described using the cumulative Weibull distribution function[38]:

$$\Phi = \begin{cases} 1 - exp\left(-\left(\frac{\eta-\eta_0}{\lambda}\right)^{\kappa}\right), & \eta \geq \eta_0 \\ 0, & \eta < \eta_0 \end{cases} \tag{14}$$

The location parameter η_0 corresponds to the critical value above which API particles can be removed from the carrier. The scale parameter λ predicts the range over which the dispersion ratio increases from 0 to 1. The shape parameter κ characterises the rate of increase of the dispersion ratio. The values of these parameters are shown in Table 2. It can be seen from Fig. 8 that the dispersion ratio increases dramatically as soon as the force ratio is larger than

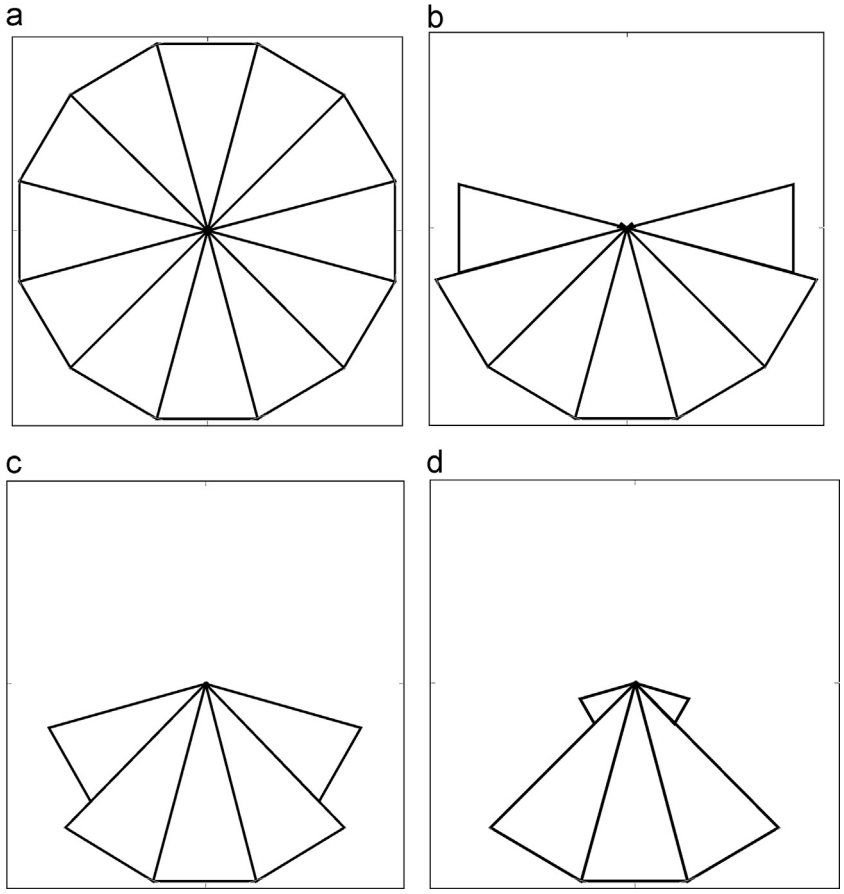

Figure 5 Polar histograms of the contact orientations distribution (R=26.25 μm, Γ=0.2 mJ/m^2). (a) V=1 m/s, (b) V=2 m/s, and (c) V=3 m/s and (d) V=4 m/s.

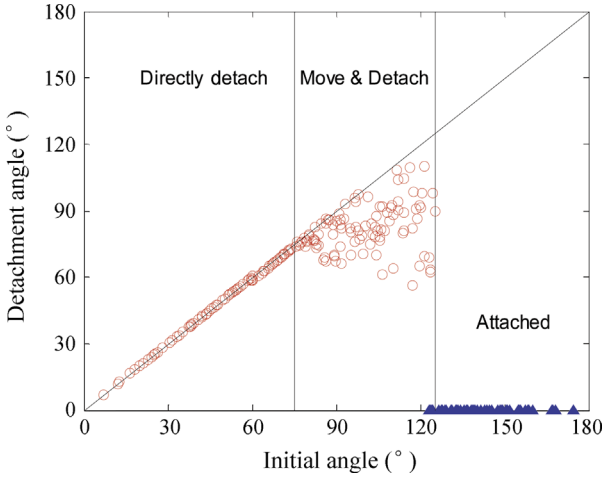

Figure 6 The variation of detachment angle with initial angle (R=26.25 μm, Γ=0.2 mJ/m^2, V=4.0 m/s).

the critical value and then asymptotically reaches 1.0 as the force ratio is further increased. Therefore, the dispersion performance can be described using Eq. (14) in the whole range in which the dispersion ratio changes between 0 and 1.

Fig. 9 illustrates the forces acting on the ith spherical API particle (Eq. (1)), in which f_{ci_n} and f_{ci_t} are the normal and tangential components of the contact force f_{ci}, respectively. Once the air flow is introduced, the air–particle interaction force f_{api} drags the API particle to a positive y position, since the component in the positive y direction of f_{api} is dominant. If the API particle is located in the upstream hemisphere of the spherical carrier particle (*i.e.*, $90^\circ \le \alpha \le 180^\circ$), the air–particle interaction force f_{api} actually compresses the API particle to the carrier. If the API particle is located in the downstream hemisphere (*i.e.*, $0^\circ \le \alpha \le 90^\circ$), the air–particle interaction forces f_{api} actually pull the API particle away from the carrier. When the normal component of the air–particle interaction force f_{api} is larger than the pull-off force F_c (Eq. (3), the API particle can be removed from the carrier. In addition, due to the effects of the tangential component of the air–particle interaction force f_{api} and the torque caused by the tangential component of the contact force, f_{ci_t}, the API particles located in the upstream hemisphere can move (either slide or roll) to the downstream hemisphere and then be removed from the carrier. This process is also clearly shown in the snapshots in Fig. 2. Therefore, the API particles in the downstream regions of the spherical carrier particle are more likely to be removed by air flow.

It is worth noting that the air flow around the carrier and the air–particle interaction forces f_{api} for API particles are not necessarily identical. The air–particle interaction forces for API particles at different positions around the carrier are determined by the local air velocities. However, since the ratio of the size of carrier to that of APIs for carrier-based formulations is normally larger than 10, even up to 20, it is challenging to determine the localised air flow

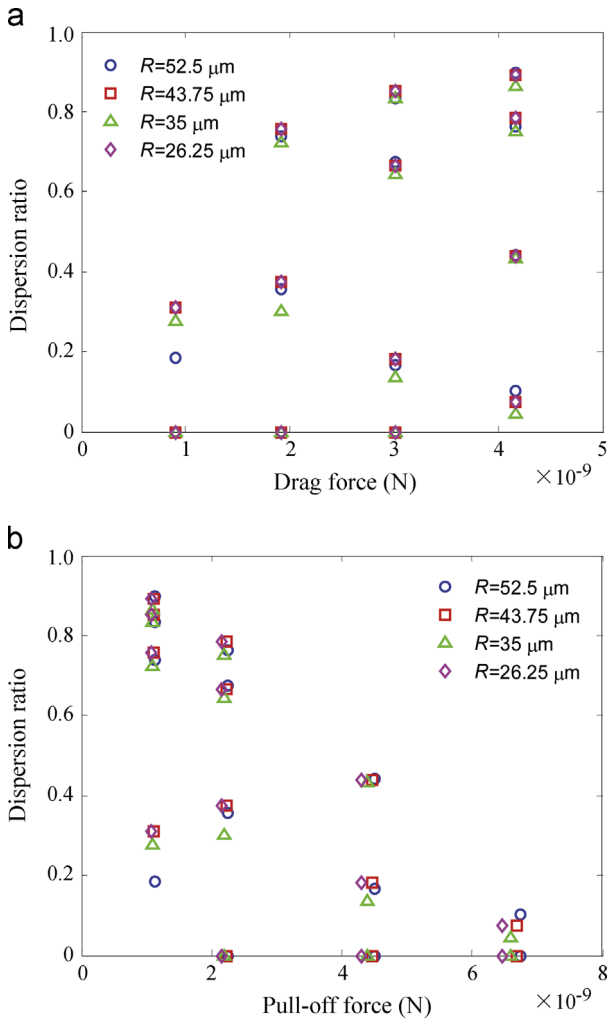

Figure 7 The variation of the dispersion ratio with the fluid drag force and the pull-off force for a range of carrier radii.

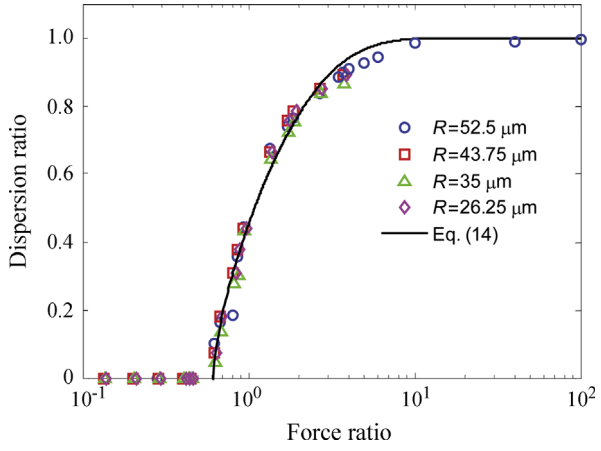

Figure 8 The variation of dispersion ratio, Φ, with the ratio of the fluid drag force to the pull-off force, η, for carrier particles with a range of radii.

at the API size level using DEM–CFD, as the fluid cell size employed in DEM–CFD is relatively large (*i.e.*, > the carrier size). In the current DEM–CFD simulations, the fluid cell is twice

Table 2 Fitting parameter.

Parameter	Value
η_0	0.61
λ	0.80
κ	0.71

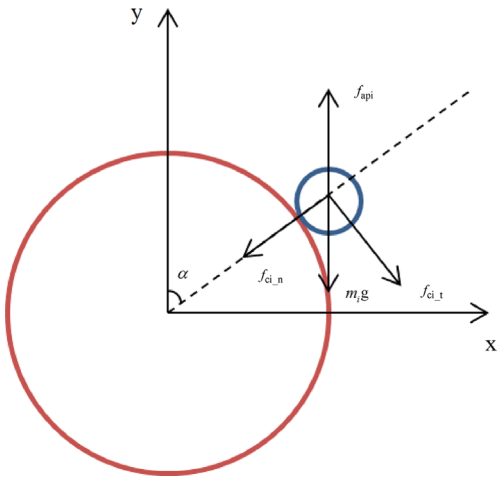

Figure 9 The forces acting on the API particle.

greater than the size of the carrier. Therefore, the air velocity around the carrier is resolved with relatively coarse fluid grids and the air–particle interaction forces f_{api} for all the API particles in the same fluid cell are almost identical. Even then, the DEM–CFD with coarse fluid grids would offer a robust tool for exploring the dispersion behaviour of DPIs with a large number of carrier-based agglomerates because of their high compute efficiency. Furthermore, a more accurate determination of f_{api} could be achieved by using the gradient interpolations proposed by Wu et al.[39] to calculate the Eulerian field quantities (*e.g.*, fluid velocity, pressure and void fraction) at the particle centre in a fluid cell. Nevertheless, further investigation is needed to employ enhanced DEM–CFD methods, such as that with immersed boundary methods[40], which enable a detailed analysis of gas–particle interactions using fine fluid cells, so that the significance of the localised fluid flow on the dispersion behaviour of carrier-based DPI formulations can be evaluated.

5. Conclusions

A coupled DEM–CFD with coarse fluid grids is applied to investigate the effect of air flow on the dispersion performance of carrier-based DPI formulations. A carrier-based agglomerate is initially formed and then dispersed in a uniformed air field. It is shown that air flow can detach the spherical API particles from the carrier after it is introduced. In addition, the particles in the downstream air flow regions are prone to be removed by the air flow.

The influence of air velocity and work of adhesion, which relate to the removal and adhesive forces, have also been examined. Since the dispersion ratio is governed by the ratio of the fluid drag force to the pull-off force, the current work suggests that DPI performance is the result of the balance of those two forces. It is

also found that the cumulative Weibull distribution function (Eq. (14)) can well describe the dispersion performance of DPIs.

Acknowledgements

The financial support from the Chinese Scholarship Council (CSC) and the School of Chemical Engineering at the University of Birmingham through the Li Siguang Scholarship Scheme is gratefully acknowledged by the first author.

References

1. Islam N, Gladki E. Dry powder inhalers (DPIs) – a review of device reliability and innovation. *Int J Pharm* 2008;**360**:1–11.
2. Smith IJ, Parry-Billings M. The inhalers of the future? A review of dry powder devices on the market today. *Pulm Pharmacol Ther* 2003;**16**:79–95.
3. Pritchard JN. The influence of lung deposition on clinical response. *J Aerosol Med* 2001;**14 Suppl 1:**S19–26.
4. Aulton ME, Taylor K. *Pharmaceutics: the science of dosage form design*. 2nd ed. Edinburgh: Churchill Livingstone; 2001.
5. Coates MS, Chan HK, Fletcher DF, Raper JA. Influence of air flow on the performance of a dry powder inhaler using computational and experimental analyses. *Pharm Res* 2005;**22**:1445–53.
6. Coates MS, Chan HK, Fletcher DF, Raper JA. Effect of design on the performance of a dry powder inhaler using computational fluid dynamics. Part 2: Air inlet size. *J Pharm Sci* 2006;**95**:1382–92.
7. Coates MS, Chan HK, Fletcher DF, Chiou H. Influence of mouthpiece geometry on the aerosol delivery performance of a dry powder inhaler. *Pharm Res* 2007;**24**:1450–6.
8. Newman SP, Busse WW. Evolution of dry powder inhaler design, formulation, and performance. *Respir Med* 2002;**96**:293–304.
9. Wong W, Fletcher DF, Traini D, Chan HK, Young PM. The use of computational approaches in inhaler development. *Adv Drug Deliv Rev* 2012;**64**:312–22.
10. Kaialy W, Alhalaweh A, Velaga SP, Nokhodchi A. Influence of lactose carrier particle size on the aerosol performance of budesonide from a dry powder inhaler. *Powder Technol* 2012;**227**:74–85.
11. Young PM, Edge S, Traini D, Jones MD, Price R, El-Sabawi D, et al. The influence of dose on the performance of dry powder inhalation systems. *Int J Pharm* 2005;**296**:26–33.
12. Kaialy W, Alhalaweh A, Velaga SP, Nokhodchi A. Effect of carrier particle shape on dry powder inhaler performance. *Int J Pharm* 2011;**421**:12–23.
13. Young PM, Roberts D, Chiou H, Rae W, Chan HK, Traini D. Composite carriers improve the aerosolisation efficiency of drugs for respiratory delivery. *J Aerosol Sci* 2008;**39**:82–93.
14. Kaialy W, Nokhodchi A. Antisolvent crystallisation is a potential technique to prepare engineered lactose with promising aerosolisation properties: effect of saturation degree. *Int J Pharm* 2012;**437**:57–69.
15. Shur J, Kubavat HA, Ruecroft G, Hipkiss D, Price R. Influence of crystal form of ipratropium bromide on micronisation and aerosolisation behaviour in dry powder inhaler formulations. *J Pharm Pharmacol* 2012;**64**:1326–36.
16. Kaialy W, Hussain T, Alhalaweh A, Nokhodchi A. Towards a more desirable dry powder inhaler formulation: large spray-dried Mannitol Microspheres outperform small Microspheres. *Pharm Res* 2013 Aug 6. Available from: http: //dx.doi.org/10.1007/s11095-013-1132-2.
17. Rabbani NR, Seville PC. The influence of formulation components on the aerosolisation properties of spray-dried powders. *J Control Release* 2005;**110**:130–40.
18. Kaialy W, Nokhodchi A. Engineered mannitol ternary additives improve dispersion of lactose–salbutamol sulphate dry powder inhalations. *AAPS J* 2013;**15**:728–43.
19. Ning Z, Boerefijn R, Ghadiri M, Thornton C. Distinct element simulation of impact breakage of lactose agglomerates. *Adv Powder Technol* 1997;**8**:15–37.
20. Calvert G, Hassanpour A, Ghadiri M. Mechanistic analysis and computer simulation of the aerodynamic dispersion of loose aggregates: effect of surface energy. In: Nakagawa M, Luding S, editors. Powders and Grains 2009: Proceedings of the 6th International Conference on Micromechanics of Granular Media. 2009 July 13–17, Golden, Colorado, US. New York: AIP Publishing; 2009, p.1047–50.
21. Yang JC, Wu CY, Adams M. DEM analysis of particle adhesion during powder mixing for dry powder inhaler formulation development. *Granul Matter* 2013;**15**:417–26.
22. Zhou QT, Tong ZB, Tang P, Citterio M, Yang RY, Chan HK. Effect of device design on the aerosolization of a carrier-based dry powder inhaler-a case study on Aerolizer® Foradile®. *AAPS J* 2013;**15**:511–22.
23. Voss A, Finlay WH. Deagglomeration of dry powder pharmaceutical aerosols. *Int J Pharm* 2002;**248**:39–50.
24. de Boer AH, Hagedoorn P, Gjaltema D, Lambregts D, Irngartinger M, Frijlink HW. The rate of drug particle detachment from carrier crystals in an air classifier-based inhaler. *Pharm Res* 2004;**21**:2158–66.
25. Calvert G, Hassanpour A, Ghadiri M. Mechanistic analysis and computer simulation of the aerodynamic dispersion of loose aggregates. *Chem Eng Res Des* 2011;**89**:519–25.
26. Wong W, Fletcher DF, Traini D, Chan HK, Crapper J, Young PM. Particle aerosolisation and break-up in dry powder inhalers 1: evaluation and modelling of venturi effects for agglomerated systems. *Pharm Res* 2010;**27**:1367–76.
27. Wong W, Fletcher DF, Traini D, Chan HK, Crapper J, Young PM. Particle aerosolisation and break-up in dry powder inhalers: evaluation and modelling of impaction effects for agglomerated systems. *J Pharm Sci* 2011;**100**:2744–54.
28. Tong ZB, Yang RY, Chu KW, Yu AB, Adi S, Chan HK. Numerical study of the effects of particle size and polydispersity on the agglomerate dispersion in a cyclonic flow. *Chem Eng J* 2010;**164**:432–41.
29. Kafui KD, Thornton C, Adams MJ. Discrete particle-continuum fluid modelling of gas-solid fluidised beds. *Chem Eng Sci* 2002;**57**:2395–410.
30. Johnson KL, Kendall K, Roberts AD. Surface energy and the contact of elastic solids. *Proc R Soc Lond A* 1971;**324**:301–13.
31. Thornton C, Yin KK. Impact of elastic spheres with and without adhesion. *Powder Technol* 1991;**65**:153–66.
32. Anderson TB, Jackson R. Fluid mechanical description of fluidized beds. Equations of motion. *Ind Eng Chem Fundamen* 1967;**6**:527–39.
33. Di Felice R. The voidage function for fluid-particle interaction systems. *Int J Multiph Flow* 1994;**20**:153–9.
34. Alderborn G, Nystrom C. *Pharmaceutical powder compaction technology*. New York: Marcel Dekker, Inc; 1996.
35. Louey MD, Mulvaney P, Stewart PJ. Characterisation of adhesional properties of lactose carriers using atomic force microscopy. *J Pharm Biomed Anal* 2001;**25**:559–67.
36. Gotoh K, Masuda H, Higashitani K. Dispersion of particles. In: Masuda H, Higashitani K, Yoshida H, editors. *Powder technology handbook*. 3rd ed. Boca Raton, FL: CRC Press; 2006, p. 449–56.
37. Zhang L. *The behaviour of granular material in pure shear, direct shear and simple shear*. Birmingham: University of Aston; 2003.
38. Papoulis A, Pillai SU. *Probability, random variables and stochastic processes*. 4th ed. Noida: McGraw-Hill Education (India) Pvt Limited; 2002.
39. Wu CL, Zhan JM, Li YS, Lam KS. Dense particulate flow model on unstructured mesh. *Chem Eng Sci* 2006;**61**:5726–41.
40. Guo Y, Wu CY, Thornton C. Modeling gas-particle two-phase flows with complex and moving boundaries using DEM-CFD with an immersed boundary method. *AIChE J* 2013;**59**:1075–87.